

Full Length Article

Enhanced quality of single crystal $\text{CrB}_x/\text{TiB}_y$ diboride superlattices by controlling boron stoichiometry during sputter deposition

Samira Dorri^{a,*}, Naureen Ghafoor^a, Justinas Palisaitis^a, Sjoerd Stendahl^b, Anton Devishvili^c, Alexei Vorobiev^{b,c}, Fredrik Eriksson^a, Per O.Å. Persson^a, Jens Birch^a

^a Thin Film Physics Division, Department of Physics, Chemistry and Biology (IFM), Linköping University, SE-581 83 Linköping, Sweden

^b Department of Physics and Astronomy, Material Physics, Uppsala University, SE-751 20 Uppsala, Sweden

^c Institut Laue-Langevin, 71 avenue des Martyrs, CS 20156, 38042 Grenoble cedex 9, France

ARTICLE INFO

Keywords:

Superlattice
Diboride
Thin film
Co-sputtering
Nanostructure

ABSTRACT

Single-crystal $\text{CrB}_2/\text{TiB}_2$ diboride superlattices with well-defined layers are promising candidates for neutron optics. However, excess B in sputter-deposited TiB_y using a single TiB_2 target deteriorates the structural quality of $\text{CrB}_x/\text{TiB}_y$ (0001) superlattices. We study the influence of co-sputtering of $\text{TiB}_2 + \text{Ti}$ on the stoichiometry and crystalline quality of 300-nm-thick TiB_y single layers and $\text{CrB}_x/\text{TiB}_y$ (0001) superlattices on Al_2O_3 (0001) substrates grown by DC magnetron sputter epitaxy at growth-temperatures T_s ranging from 600 to 900 °C. By controlling the relative applied powers to the TiB_2 and Ti magnetrons, y could be reduced from 3.3 to 0.9. $\text{TiB}_{2.3}$ grown at 750 °C exhibited epitaxial domains about 10x larger than non-co-sputtered films. Close-to-stoichiometry $\text{CrB}_{1.7}/\text{TiB}_{2.3}$ superlattices with modulation periods $\Lambda = 6$ nm grown at 750 °C showed the highest single crystal quality and best layer definition. $\text{TiB}_{2.3}$ layers display rough top interfaces indicating kinetically limited growth while $\text{CrB}_{1.7}$ forms flat and abrupt top interfaces indicating epitaxial growth with high adatom mobility.

1. Introduction

Single crystal, hetero-epitaxially grown periodic multilayers, also known as superlattices (SLs), have great potential for highly efficient interference neutron mirrors at large-scale neutron facilities owing to the possibility of achieving extremely abrupt interfaces ($\pm \frac{1}{2}$ atomic layer). CrB_2 and TiB_2 exhibit a small lattice mismatch (1.92 % along the a -axis) and a large difference in neutron scattering cross section which make $\text{CrB}_2/\text{TiB}_2$ SLs a suitable candidate for neutron optics. Hence, for this application, it is crucial to obtain high-quality single crystal SLs with periodicities ($\Lambda = D_{\text{CrB}_2} + D_{\text{TiB}_2}$) in the range of 1–100 nm with as abrupt interfaces as possible.

We previously demonstrated the possibility of growing relatively high-crystalline-quality $\text{CrB}_x/\text{TiB}_y$ (0001) diboride SLs [$x, y \in 1.7\text{--}3.3$] on Al_2O_3 (0001) substrates by magnetron sputter epitaxy (MSE) [1]. However, over-stoichiometric $\text{TiB}_{3.3}$, and the formation of B-rich tissue phases, particularly for SLs with layer-thickness ratios $\Gamma = \frac{D_{\text{TiB}_y}}{D_{\text{CrB}_x} + D_{\text{TiB}_y}} \geq 0.5$, was found to cause deterioration of the epitaxy and interface quality [1]. Hence, controlling the B stoichiometry is key to obtain high-quality

epitaxial growth of $\text{CrB}_x/\text{TiB}_y$ SLs with flat and abrupt interfaces. Due to the differences between sputter-ejected target constituents, where sputtered B atoms are preferentially ejected along the target surface normal, while sputtered Ti atoms have a wider angular ejection distribution with a relatively higher off-normal flux [2], sputter-deposited TiB_y are typically over-stoichiometric ($\text{B}/\text{Ti} > 2$) [3–6]. Some methods were proposed to control the compositions of over-stoichiometric monolithic TiB_2 thin films [2,7–9]. However, they merely focus on tuning the composition of polycrystalline and nanostructured single-phase thin films rather than the crystalline quality and are not suited for growing $\text{CrB}_x/\text{TiB}_y$ SL neutron mirrors engineered with sub-nm layer thickness precision. A method to control the TiB_y stoichiometry should not negatively affect the epitaxial growth and composition of the CrB_x layers, for which good growth conditions for the composition ($x = \text{B}/\text{Cr}$ ratio = 1.7 for $\text{CrB}_{1.7}$ single layers) and crystalline quality have already been established [1]. Recently, the interest in transition metal diboride SLs for hard-coating applications has also increased owing to a possible improvement in mechanical properties through the hindering of dislocation mobility at the interfaces [10]. Mechanical properties of $\text{TiB}_2/$

* Corresponding author.

E-mail address: samira.dorri@liu.se (S. Dorri).

<https://doi.org/10.1016/j.apsusc.2024.159606>

Received 6 December 2023; Received in revised form 23 January 2024; Accepted 2 February 2024

Available online 5 February 2024

0169-4332/© 2024 The Author(s). Published by Elsevier B.V. This is an open access article under the CC BY license (<http://creativecommons.org/licenses/by/4.0/>).

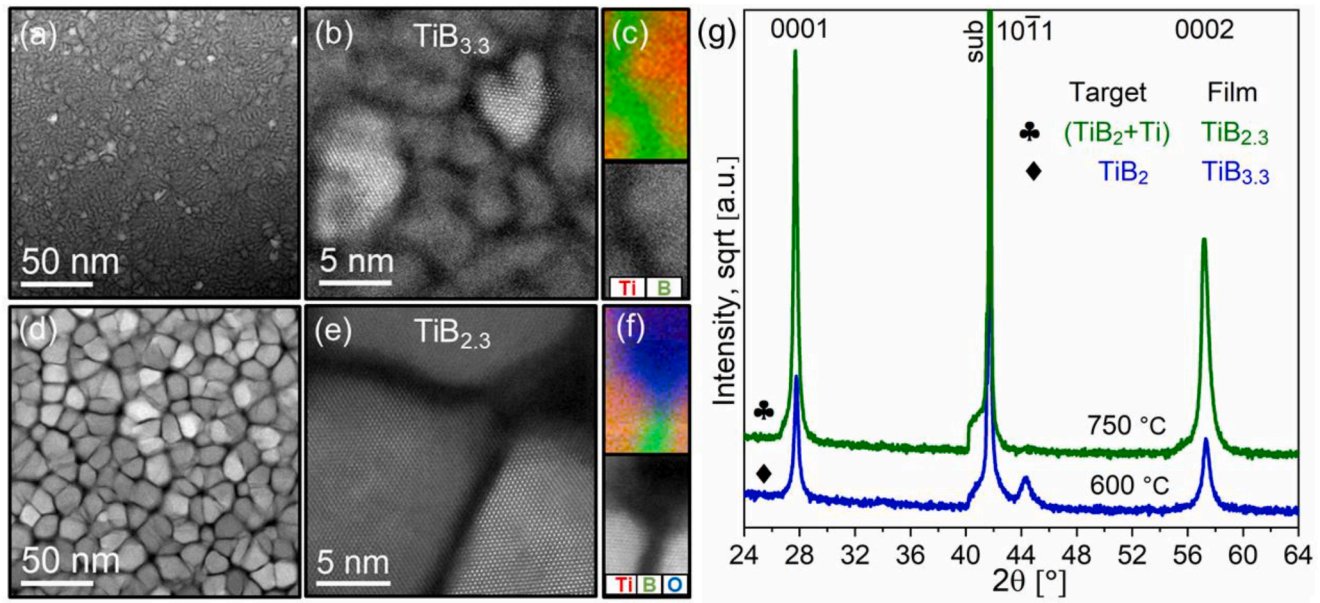


Fig. 1. (a, b, c) show HAADF-STEM micrographs of non-co-sputtered $\text{TiB}_{3.3}$ at $T_s = 600^\circ\text{C}$ and (d, e, f) co-sputtered $\text{TiB}_{2.3}$ at $T_s = 750^\circ\text{C}$: (a and d) low-magnification, (b and e) lattice-resolved plan-view micrographs, and (c and f) EELS map of Ti-L_{2,3} (red), B-K (green), and O-K (blue) in $\text{TiB}_{3.3}$ and $\text{TiB}_{2.3}$. (g) corresponding XRD θ - 2θ scans for 300-nm-thick $\text{TiB}_{3.3}$ and $\text{TiB}_{2.3}$ single layers grown at $T_s = 600$ and 750°C , respectively. (For interpretation of the references to color in this figure legend, the reader is referred to the web version of this article.)

WB_2 and $\text{TiB}_2/\text{ZrB}_2$ polycrystalline SLs have been studied which showed over-stoichiometric $\text{TiB}_{2.66}$ [11], further underlining the importance of controlling the B stoichiometry for better crystalline quality metal diboride SLs. Hellgren et al. [12] showed that the B/Ti ratio of TiB_y thin films co-sputtered from Ti and TiB_2 targets can be tuned from $y = 2.8$ to 1.2 by increasing the Ti-target power while maintaining the TiB_2 -target power constant. However, the as-deposited layers were amorphous, and a high-temperature (1100°C) vacuum-annealing process was essential to achieve polycrystalline thin films. In this work, we explore a strategy for achieving high crystal quality $\text{CrB}_2/\text{TiB}_2$ SLs, with emphasis on obtaining the highest possible layer definition, by employing co-sputtering from TiB_2 and Ti targets to control the B stoichiometry, y , in TiB_y , at substrate temperatures between 600 and 900°C .

2. Material and methods

0001-oriented TiB_y single layers and $\text{CrB}_x/\text{TiB}_y$ superlattices (SLs) were grown in a direct-current MSE system on $\text{Al}_2\text{O}_3(0001)$ substrates. The deposition system is equipped with two type II 7.5-cm-diameter unbalanced magnetrons with a tilt angle of 25° and one 5-cm-diameter balanced magnetron with a tilt angle of 50° to the substrate normal, which are mounted in a confocal geometry at the top of the chamber. Stoichiometric 7.5-cm CrB_2 and TiB_2 compound targets, and a 5-cm Ti metal target (99.9 % purity) were used. The substrates were mounted on a substrate table below the magnetrons at a target-to-substrate distance of about 12 cm, rotating at a constant rate of 17 rpm in order to ensure good lateral thickness uniformity of the deposited layers. All three magnetrons were continuously running during the deposition, and fast computer-controlled shutters were used in front of each target to obtain the desired layer thicknesses. The base pressure for the deposition system was 3×10^{-7} Torr. Polished $\text{Al}_2\text{O}_3(0001)$, $1.0 \times 1.0 \text{ cm}^2$, substrates were chemically cleaned sequentially in trichloroethylene (3 min), acetone (5 min), and isopropanol (5 min) in an ultrasonic bath, and then blown dry with pure nitrogen before inserting the substrates through a load-lock into the deposition chamber.

All substrates were pre-heated in vacuum at 900°C for about one hour before deposition to produce a clean well-ordered surface. A negative bias voltage of -30 V was applied to the substrate to attract

ions from the plasma. To further enhance the ion flux a solenoid surrounding the substrate which dynamically coupled to the magnetic field of each of the type II magnetrons was utilized [13]. A series of 300-nm-thick single-layer thin films were synthesized by co-sputtering of Ti and TiB_2 at $T_s = 600^\circ\text{C}$ and $p_{\text{Ar}} = 4 \text{ mTorr}$ which are the optimum growth conditions for depositing $\text{CrB}_x/\text{TiB}_y$ SLs [11]. The relative powers to the TiB_2 and Ti magnetrons were varied from 120 to 70 W and 0 to 50 W, respectively, at a constant total power of $P_{\text{TiB}_2} + P_{\text{Ti}} = 120 \text{ W}$. Selected TiB_y single layers were grown at $T_s = 750^\circ\text{C}$ and 900°C . A first series of $\text{CrB}_x/\text{TiB}_y$ SLs with a modulation period of $\Lambda = 6 \text{ nm}$, thickness ratio $\Gamma = \frac{D_{\text{TiB}_y}}{\Lambda} \approx 0.7$, and $N = 50$ bilayers was studied using co-sputtering for TiB_y layers with $P_{\text{Ti}} = 20$ and 25 W, at two different growth temperatures $T_s = 600^\circ\text{C}$ and 750°C . A second series of SLs with different thickness ratios $\Gamma \approx 0.3, 0.5$, and 0.7 was deposited at a substrate temperature of $T_s = 750^\circ\text{C}$ with $\Lambda = 6 \text{ nm}$, $N = 50$, at the optimum applied power of $P_{\text{TiB}_2}/P_{\text{Ti}} = 100 \text{ W}/20 \text{ W}$. For growing SLs, the applied power to the CrB_2 target was 80 W, yielding a CrB_x deposition rate of 0.066 nm/s . For TiB_y with $P_{\text{Ti}} = 20\text{--}25 \text{ W}$ and a constant total power of $P_{\text{TiB}_2} + P_{\text{Ti}} = 120 \text{ W}$, the deposition rate was $0.055 \pm 0.005 \text{ nm/s}$. Information about how to calculate the deposition rate in SL structures is described in [14].

X-ray diffraction (XRD) θ - 2θ was performed using a Panalytical X'Pert Bragg-Brentano diffractometer with a Cu X-ray source, operating at 45 kV and 40 mA, generating Cu- K_α X-rays. On the primary side a Bragg-Brentano HD mirror was used with a $\frac{1}{2}^\circ$ divergence slit and a $\frac{1}{2}^\circ$ antiscatter slit, and on the secondary side a 5-mm antiscatter slit was used together with an X'celerator detector operating in scanning line mode. The elemental compositions of the films were determined using time-of-flight elastic recoil detection analysis (ToF-ERDA) and was carried out with a 36 MeV $^{127}\text{I}^{8+}$ probe beam incident at 67.5° with respect to the sample surface normal and the recoils were detected at an angle of 45° [15]. The Linköping double-corrected FEI Titan³ 60–300 microscope, operated at 300 kV was used for (scanning) transmission electron microscopy ((S)TEM) studies. The microstructure and local composition were investigated by STEM high angle annular dark field (HAADF-STEM) imaging and electron energy loss spectroscopy (EELS). Cross-sectional TEM sample preparation was performed using mechanical polishing followed by Ar ion milling. Plan-view TEM samples were prepared by conventional cutting and cleaving followed by a gentle

focused ion beam (FIB) milling [16]. X-ray reflectivity (XRR) was performed using a Panalytical Empyrean diffractometer with a Cu X-ray tube, operating at 45 kV and 40 mA. On the primary side, a parallel beam X-ray mirror was used in combination with a $1/32^\circ$ divergence slit and a parallel plate collimator was used in combination with a collimator slit at the reflected beam using a PIXcel-3D area detector in 0D mode. Neutron reflectivity (NR) was conducted at the Institut Laue-Langevin in Grenoble with the Swedish neutron reflectometer Super-ADAM [17]. The measurement was performed using a monochromatic wavelength of 5.183 Å and a sample-to-detector distance of 250 cm. Footprint correction was applied using dedicated data reduction software at the beamline.

3. Results and discussion

To explore if co-sputtering of TiB_2 and Ti can dilute the amount of B in the over-stoichiometric TiB_y layers without causing any amorphization, a series of TiB_y single layers were grown with different relative applied power to the Ti and TiB_2 targets at $T_S = 600^\circ\text{C}$, and evaluated with respect to composition and quality as presented in Supplementary Materials (SM). The y value in TiB_y was gradually decreased from 3.3 to 0.9 by increasing the relative applied power to the Ti vs. TiB_2 target. $\text{TiB}_{2.3}$ gave optimal crystalline quality and stoichiometry (Fig. S1 in SM). The crystalline quality of $\text{TiB}_{2.3}$ further improved by increasing T_S up to 750°C , as discussed and shown in Fig. S2 in SM.

Fig. 1 (a-f) compare plan-view HAADF-STEM micrographs and color-coded Ti-L₂₃ (red), B-K (green), and O-K (blue) EELS elemental maps from the non-co-sputtered TiB_{3.3} grown at T_s = 600 °C and co-sputtered TiB_{2.3} grown at T_s = 750 °C. Low-magnification and lattice-resolved plan-view micrographs of TiB_{3.3} in **Fig. 1**(a) and 1(b) show bright contrast crystalline domains embedded in a matrix of low-density. The corresponding EELS map in **Fig. 1**(c) indicate that the excess B in this single layer segregates to the column boundaries, forming an amorphous B-rich tissue phase. This is a typical nanostructure of TiB₂ thin films grown by magnetron sputtering [18,19].

Fig. 1(a) and 1(d) show that crystalline domains in $\text{TiB}_{2.3}$ are approximately ten times larger across, than those in the highly over-stoichiometric $\text{TiB}_{3.3}$. The lattice-resolved images in Fig. 1(b) and 1(e) reveal that the larger domains in $\text{TiB}_{2.3}$ are single crystalline in nature, exhibiting clear lattice fringes in all domains, showing a higher degree of crystalline order than in $\text{TiB}_{3.3}$. Fig. 1(f) shows EELS elemental map from a junction between multiple domain boundaries in $\text{TiB}_{2.3}$. The map indicates that the boundaries are B rich, while the junctions are O rich, proving the formation of large porosities along boundary junctions where atmospheric oxygen can enter the porous $\text{TiB}_{2.3}$, possibly deteriorating the film properties [20]. This is supported by ToF-ERDA that shows 9 at. % O in the $\text{TiB}_{2.3}$ single layer grown at $T_S = 750^\circ\text{C}$, as compared to 1.6 at. % O in the $\text{TiB}_{3.3}$ layer.

Fig. 1(g) shows the corresponding XRD θ -2 θ scans of TiB_{3.3} and TiB_{2.3} single layers. Comparatively higher intensity of the 000 l peaks in TiB_{2.3} and absence of 10 $\bar{1}$ 1-oriented crystallites indicate higher crystalline quality than for the TiB_{3.3} owing to the reduced amount of B in the film.

After achieving high crystalline quality $\text{TiB}_{2.3}$ by co-sputtering at $T_S = 750^\circ\text{C}$, we investigated its impact on improving epitaxial growth of 000l-oriented $\text{CrB}_x/\text{TiB}_y$ SLs on c-plane sapphire. Without employing Ti co-deposition, $\text{CrB}_x/\text{TiB}_y$ SLs with highly non-stoichiometric individual layers were obtained at an optimum temperature of $T_S = 600^\circ\text{C}$ [1]. The established, considerably higher, optimum growth temperature for $\text{TiB}_{2.3}$ by Ti co-sputtering, implies that a higher T_S may be expected also for SLs. In addition to $y = 2.3$, the lower B/Ti ratio $y = 2.1$, established for TiB_y single layers, would be of interest for SLs for achieving a closer-to-stoichiometry composition. Thus, a series of $\text{CrB}_x/\text{TiB}_y$ SLs were grown using $\text{TiB}_2 + \text{Ti}$ co-sputtering with the optimal deposition parameters for $\text{TiB}_{2.3}$ and $\text{TiB}_{2.1}$, at two different growth temperatures $T_S = 600$ and 750°C with the modulation period $\Lambda = 6$ nm and thickness

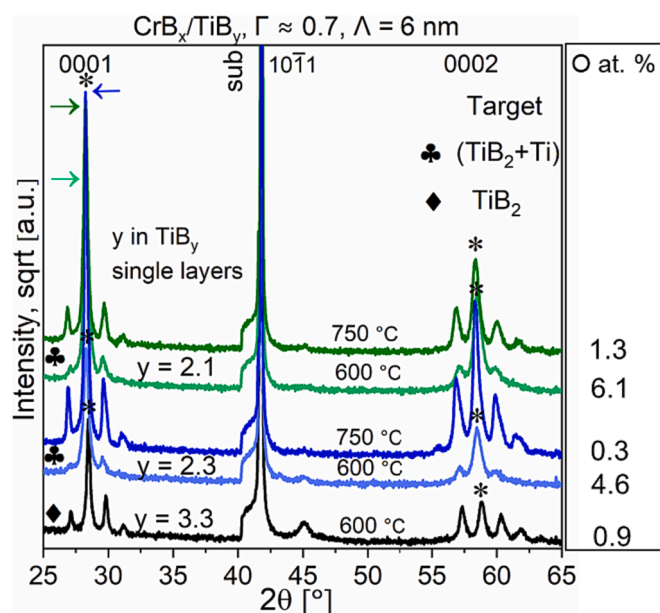


Fig. 2. XRD θ -2 θ scans for superlattices with different y values corresponding to TiB₂ single layers, grown at $T_s = 600$ and 750 °C. Modulation period $\Lambda = 6$ nm, thickness ratio $\Gamma \approx 0.7$, and number of bilayers $N = 50$ were kept constant. The average 000 l superlattice peaks are marked by (*).

ratio of $\Gamma = \frac{D_{\text{TiBy}}}{\Lambda} \approx 0.7$. For comparison, a SL with the same Λ and Γ was grown without Ti co-sputtering at $T_s = 600^\circ\text{C}$ (the same growth conditions as in [11]). The large relative thickness of TiBy $\Gamma \approx 0.7$ was chosen to give a large impact on reducing excess B leading to an improved nanostructure by co-sputtering. Fig. 2 shows the XRD θ -2 θ data of $\text{CrB}_y/\text{TiB}_y$ SLs for $y = 3.3, 2.3$, and 2.1 , corresponding to TiB_y single layers. The intensities of the 0001 and 0002 SLs average peaks (marked by * in the figure) and the intensities and number of visible satellite peaks, indicate that the SL grown at $T_s = 750^\circ\text{C}$ with $\text{TiB}_{2.3}$ has the highest crystalline quality.

Compositional analyses show that the average B/transition metal (TM) ratio for the co-sputtered SLs is about 2.1, and for the non-co-sputtered SL is 2.7. In addition, there is a considerable decrease in the oxygen concentration (see in Fig. 2) from 4.6 at. % to 0.3 at. % when increasing T_S from 600 °C to 750 °C in SLs with $\text{TiB}_{2.3}$. A slightly higher oxygen concentration with a similar decreasing effect (from 6.1 at. % to 1.3 at. %) upon increasing T_S is observed for SLs grown with optimum deposition parameters for $\text{TiB}_{2.1}$ layers. The reduced oxygen content is attributed to a higher crystalline quality of SLs grown at 750 °C (for both $y = 2.3$ and 2.1) compared to those grown at 600 °C. This is in qualitative agreement with the observations of reduced oxygen content with improved crystal quality upon increased growth temperature as observed in ZrB_2 epilayers [21].

The SL grown from a single TiB₂ target exhibits an oxygen concentration of 0.9 at. % which is much lower than SLs synthesized at the same temperature T_S = 600 °C using co-sputtering. This may be explained by the elimination of O-rich free volume by segregation of excess B from the TiB_{3.3} layers to triple points and domain boundaries which is known to occur in CrB_x/TiB_y SLs grown under these conditions [1]. A higher layer definition in SLs synthesized using single TiB₂ target compared to the SLs co-sputtered at T_S = 600 °C is supported by the observation of more intense and higher order satellite peaks around the 000*l* average crystal peaks. However, this SL exhibits a poor crystalline quality as evidenced by low intensities of the average SL crystal peaks, the emergence of an additional peak indicating partial 10 $\bar{1}$ 1 orientation, and with a B/TM ratio of 2.7. Hence, it is unfavourable compared to the close-to-stoichiometric SL grown at T_S = 750 °C which, based on the XRD, exhibits superior crystal quality and SL layer definition. Therefore, SLs

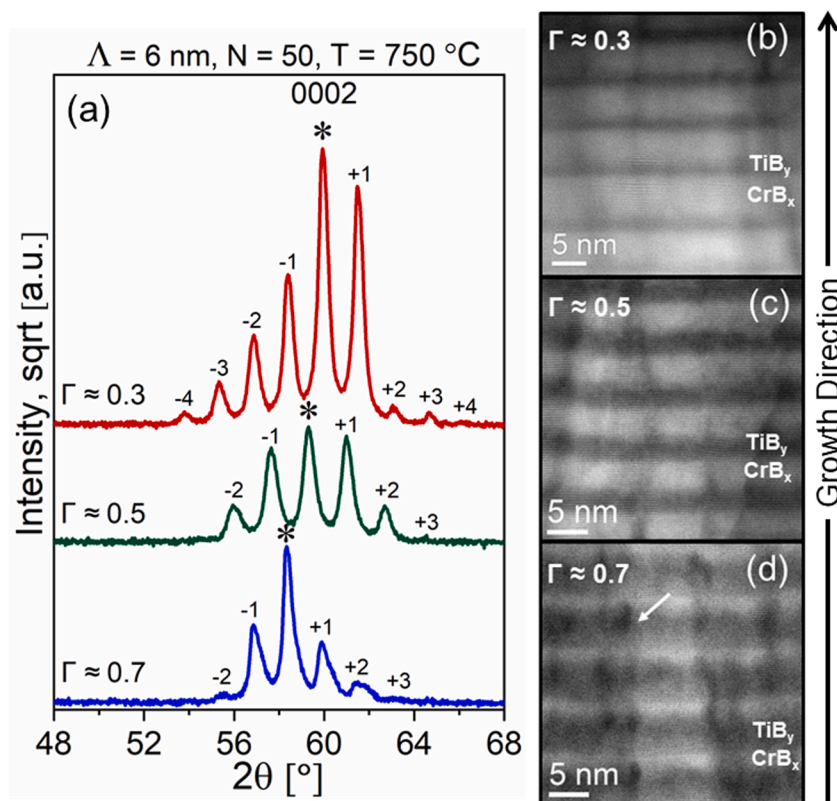


Fig. 3. (a) XRD θ -2 θ scans for $\text{CrB}_{1.7}/\text{TiB}_{2.3}$ superlattices with different thickness ratios $\Gamma \approx 0.7, 0.5$, and 0.3 . Period $\Lambda = 6$ nm and number of layers $N = 50$ were kept constant. The average 0002 superlattice peaks are marked by (*) and the order of satellites are shown by \pm integers. (b, c, d) cross-sectional HAADF-STEM micrographs of $\text{CrB}_{1.7}/\text{TiB}_{2.3}$ superlattices (corresponding to (a)) with $\Gamma \approx 0.3, 0.5$, and 0.7 .

with high structural quality and close-to-stoichiometry composition can be achieved by applying the optimized Ti and TiB_2 growth conditions for synthesizing TiB_y single layers with $y = 2.3$ at $T_s = 750$ °C. The oxygen concentration in this SL (0.3 at. %) is significantly less than that in single layer $\text{TiB}_{2.3}$ (9.0 at. %), which is due to a change from porous columnar epitaxial growth to a dense 2D epilayer growth, by the periodic introduction of CrB_x layers which are grown with a relatively higher adatom mobility, as discussed below.

Fig. 3(a) shows XRD θ -2 θ patterns of $\text{CrB}_{1.7}/\text{TiB}_{2.3}$ SLs with different thickness ratios $\Gamma \approx 0.7, 0.5$, and 0.3 , and a nominal periodicity of $\Lambda = 6$ nm for 50 bilayers $N = 50$, grown at the established optimal $T_s = 750$ °C. The high intensity of the average 0002 Bragg-peaks reveals high crystalline quality for all three thickness ratios. The $\Gamma \approx 0.3$ SL exhibits a significantly higher 0002 Bragg-peak, surrounded by a higher number and more intense satellites, indicative of higher structural quality with more well-defined layers than the SLs with relatively thicker $\text{TiB}_{2.3}$ layers ($\Gamma \geq 0.5$). In Fig. 3(b-d), cross-sectional HAADF-STEM micrographs of SLs with $\Gamma \approx 0.3, 0.5$, and 0.7 are shown. The micrographs show the presence of flat layers with relatively abrupt interfaces between the individual layers in the SLs with different thickness ratios where bright and dark layers correspond to $\text{CrB}_{1.7}$ and $\text{TiB}_{2.3}$, respectively. The darker regions (one of them marked with an arrow in Fig. 3 (d)) are B-rich tissue phases which are attributed to B segregation in the over-stoichiometric $\text{TiB}_{2.3}$ layers [1]. In Fig. 3(b) the SL with $\Gamma \approx 0.3$ exhibits only faint indication of B segregation and overall very flat layers which, together with the strong XRD SL peaks (Fig. 3(a)), is evidence of significant improvements in both crystal quality and layer definition of the SL by reducing the B stoichiometry in the TiB_y layers to $y = 2.3$, as compared to $y = 3.3$ in previous work. By the same comparison, B segregation and crystal quality are significantly improved also for $\Gamma \approx 0.5$ and 0.7 , although it is seen in Fig. 3(c and d) that the excess B in the $\text{TiB}_{2.3}$ layers causes more severe B segregation and crystal quality

deterioration as the overall B content in the SLs increases with higher $\text{TiB}_{2.3}$ relative thickness. No roughness accumulation is observed in the low-magnification STEM micrographs (not shown) of these SLs. For all three Γ s, it is clearly seen in Fig. 3(b-d) that interfaces where $\text{CrB}_{1.7}$ is over-grown by $\text{TiB}_{2.3}$ are more abrupt than the $\text{TiB}_{2.3}$ -to- $\text{CrB}_{1.7}$ interfaces.

In contrast to HAADF-STEM, XRR and NR measurements include a large sample volume and the interface quality can be quantified by corresponding simulations. In Fig. 4, the XRR and NR data of the SL with $\Lambda = 6$ nm and $\Gamma \approx 0.3$ (same as the HAADF-STEM shown in Fig. 3(b)) are shown along with the best fit simulations using the GenX code [22]. High intensity Bragg-peaks in both XRR (Fig. 4(a)) and NR (Fig. 4(b)) indicate well defined SL layers with abrupt interfaces which is in qualitative agreement with the observed XRD pattern in Fig. 3(a). The simulations were performed using the same model for both XRR and NR with coupled structural parameters for simultaneous fitting, and they show an excellent agreement with the experimental data regarding the period Λ and thickness ratio Γ . To obtain a good fit, an increasing interface width σ for each subsequent period throughout the SL stack was included in the model in order to take into account accumulated roughness resulting in reduced reflected intensity. The initial interface widths σ near the substrate, averaged over the 1.0×1.0 cm², of the $\text{CrB}_{1.7}$ -to- $\text{TiB}_{2.3}$ and $\text{TiB}_{2.3}$ -to- $\text{CrB}_{1.7}$ interfaces are found to be 0.4 Å and 1.0 Å, respectively, with interface width evolutions of 0.27 Å/period for $\text{CrB}_{1.7}$ -to- $\text{TiB}_{2.3}$ and 0.66 Å/period for $\text{TiB}_{2.3}$ -to- $\text{CrB}_{1.7}$.

The asymmetric interface widths and their evolution during SL growth observed by TEM and revealed by XRR and NR, indicate significantly different conditions for nucleation and growth of $\text{TiB}_{2.3}$ and $\text{CrB}_{1.7}$. The $\text{CrB}_{1.7}$ exhibits 2D growth which provides flat surfaces for $\text{TiB}_{2.3}$ nucleation forming abrupt interfaces. Each $\text{TiB}_{2.3}$ layer is observed to develop a rough surface, which is most pronounced for thicker $\text{TiB}_{2.3}$ layers, which then are smoothed by subsequent 2D

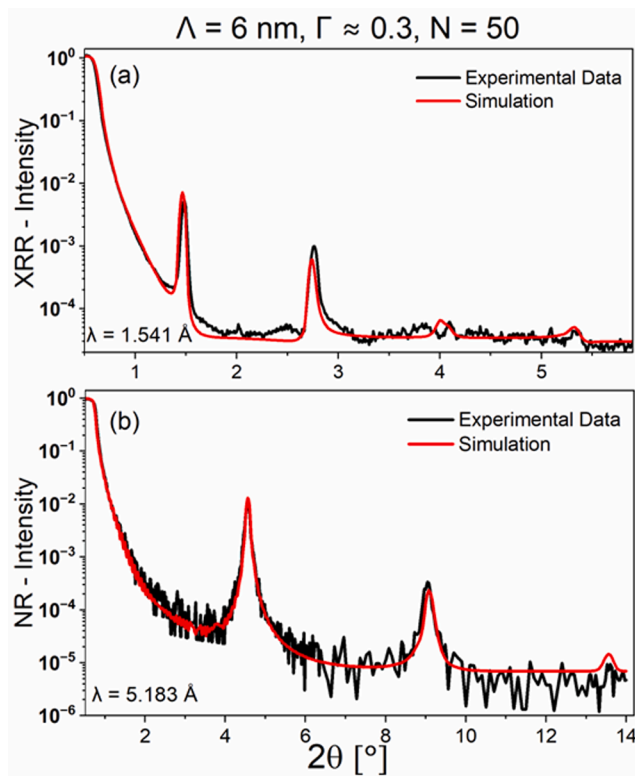


Fig. 4. XRR (a) and NR (b) data for a $\text{CrB}_{1.7}/\text{TiB}_{2.3}$ superlattice with thickness ratios $\Gamma \approx 0.3$, modulation period $\Lambda = 6$ nm and number of layers $N = 50$. The obtained best fits for both XRR and NR simulations are shown in red. The simulations were performed simultaneously for both X-ray and neutron data with coupled structural parameters (see main text for details). (For interpretation of the references to color in this figure legend, the reader is referred to the web version of this article.)

growth of $\text{CrB}_{1.7}$. We submit that such a growth scenario is possible by noting a large difference in homologous temperature (T_H) between CrB_2 and TiB_2 at $T_S = 750^\circ\text{C}$ ($T_{H\text{CrB}_2} = 0.4$ and $T_{HTiB_2} = 0.3$), where $T_H = (T_S/T_M)$ and T_M = absolute melting temperature, that would lead to a kinetically limited growth of $\text{TiB}_{2.3}$, while the $\text{CrB}_{1.7}$ growth is characterized by a high adatom mobility. That would place the $\text{CrB}_{1.7}$ close to the sweet spot for ion-assisted epitaxial growth in the Thornton structure zone diagram [23] modified by Anders [24], while the high T_M for $\text{TiB}_{2.3}$ places it in the region characterized by columnar grain growth. This model may also explain how high-quality epitaxial growth of $\text{CrB}_{1.7}/\text{TiB}_{2.3}$ SLs are obtained while growth of $\text{TiB}_{2.3}$ single layer occurs in a porous columnar epitaxial fashion under the same conditions.

4. Conclusions

Co-sputtering from Ti and TiB_2 targets provides significant control over the B content in TiB_y ($0.9 \leq y \leq 3.3$), enabling the growth of high crystal quality $\text{CrB}_x/\text{TiB}_y$ (0001) diboride superlattices (SLs). Close-to-stoichiometry single layer $\text{TiB}_{2.3}$ grown at 750°C represents the optimum growth conditions producing a columnar epitaxial film with a high (9 at. %) oxygen content due to porous column boundaries. The same growth conditions yield single crystal growth of $\text{CrB}_{1.7}/\text{TiB}_{2.3}$ (0001)/ Al_2O_3 (0001) SLs with an oxygen content of only 0.4 at. % which is attributed to a transition from a 3D columnar growth mode for single layer $\text{TiB}_{2.3}$, to a dense epitaxial 2D growth when introducing nm-thin $\text{CrB}_{1.7}$ layers, featuring a relatively high adatom mobility, to form SLs. Within the SLs, $\text{TiB}_{2.3}$ layers display rough top interfaces indicating a kinetically limited growth, while $\text{CrB}_{1.7}$ forms layers with flat and abrupt top interfaces with a smoothening effect, indicating epitaxial

growth with high adatom mobility. The rough top surfaces of the $\text{TiB}_{2.3}$ layers results in locally abrupt interfaces with an accumulating roughness evolution. The structural analyses show that SLs grown at 750°C exhibit the highest crystalline quality and the highest layer definition.

CRediT authorship contribution statement

Samira Dorri: Writing – review & editing, Writing – original draft, Project administration, Methodology, Investigation, Formal analysis, Data curation, Conceptualization. **Naureen Ghafoor:** Writing – review & editing, Data curation. **Justinas Palisaitis:** Writing – review & editing, Investigation, Data curation. **Sjoerd Stendahl:** Data curation, Investigation, Writing – review & editing. **Anton Devishvili:** Formal analysis, Investigation, Writing – review & editing. **Alexei Vorobiev:** Data curation, Formal analysis, Writing – review & editing. **Fredrik Eriksson:** Writing – review & editing, Data curation. **Per O.Å. Persson:** Writing – review & editing, Funding acquisition, Data curation. **Jens Birch:** Writing – review & editing, Supervision, Investigation, Funding acquisition, Formal analysis, Data curation, Conceptualization.

Declaration of competing interest

The authors declare that they have no known competing financial interests or personal relationships that could have appeared to influence the work reported in this paper.

Data availability

Data will be made available on request.

Acknowledgments

The authors acknowledge financial support from Swedish National Graduate School in Neutron Scattering (SwedNess), Swedish Foundation for Strategic Research (SSF) GS15 - 0008, Swedish Government Strategic Research Area in Materials Science on Advanced Functional Materials (AFM) at Linköping University (Faculty Grant SFO Mat LiU No. 2009 00971), Center in Nanoscience and technology at LiTH CeNano, Hans Werthén Foundation (IVA), Society of Vacuum Coaters Foundation (SVCF), Swedish Research Council (VR) Grant numbers 2019-00191 (for accelerator-based ion-technological center in tandem accelerator laboratory in Uppsala University), VR and SSF for access to ARTEMI, the Swedish National Infrastructure in Advanced Electron Microscopy (2021-00171 and RIF21-0026), Knut and Alice Wallenberg Foundation for the support of the electron microscopy laboratory at Linköping University (KAW 2015.0043), VR 2021-00159 for the Swedish neutron reflectometer SuperADAM at ILL 10.5291/ILL-DATA.CRG-2964, and Plansee GmbH for providing diboride targets.

Appendix A. Supplementary data

Supplementary data to this article can be found online at <https://doi.org/10.1016/j.apsusc.2024.159606>.

References

- [1] S. Dorri, J. Birch, F. Eriksson, J. Palisaitis, P.O. Persson, B. Bakht, L. Hultman, N. Ghafoor, Effects of stoichiometry and individual layer thickness ratio on the quality of epitaxial $\text{CrB}_x/\text{TiB}_y$ superlattice thin films, *Mater. Des.* (2023) 111842.
- [2] J. Neidhardt, S. Mráz, J.M. Schneider, E. Strub, W. Böhne, B. Liedke, W. Möller, C. Mitterer, Experiment and simulation of the compositional evolution of Ti–B thin films deposited by sputtering of a compound target, *J. Appl. Phys.* 104 (6) (2008) 063304.
- [3] T. Wojcik, V. Ott, S. Özbilen, H. Leiste, S. Ulrich, P.H. Mayrhofer, H. Riedl, M. Stueber, Magnetron sputtered NiAl/TiB_x multilayer thin films, *J. Vac. Sci. Technol. A* 40 (2022) 033410.
- [4] M. Mikula, B. Grančič, T. Roch, T. Plecenik, I. Vávra, E. Dobročka, A. Satka, V. Buršíková, M. Držfík, M. Zahoran, A. Plecenik, P. Kús, The influence of low-

- energy ion bombardment on the microstructure development and mechanical properties of TiB_x coatings, *Vacuum* 85 (9) (2011) 866–870.
- [5] F. Kunc, J. Musil, P.H. Mayrhofer, C. Mitterer, Low-stress superhard Ti-B films prepared by magnetron sputtering, *Surf. Coat. Technol.* 174–175 (2003) 744–753.
 - [6] M. Stüber, H. Riedl, T. Wojcik, S. Ulrich, H. Leiste, P.H. Mayrhofer, Microstructure of Al-containing magnetron sputtered TiB_2 thin films, *Thin Solid Films* 688 (2019) 137361.
 - [7] I. Petrov, A. Hall, A.B. Mei, N. Nedfors, I. Zhirkov, J. Rosen, A. Reed, B. Howe, G. Greczynski, J. Birch, L. Hultman, J.E. Greene, Controlling the boron-to-titanium ratio in magnetron-sputter-deposited TiB_x thin films, *J. Vac. Sci. Technology A: Vacuum, Surfaces, and Films* 35 (5) (2017) 050601.
 - [8] B. Bakht, I. Petrov, J.E. Greene, L. Hultman, J. Rosén, G. Greczynski, Controlling the B/Ti ratio of TiB_x thin films grown by high-power impulse magnetron sputtering, *J. Vac. Sci. Technol. A: Vacuum, Surfaces, and Films* 36 (3) (2018) 030604.
 - [9] J. Thörnberg, J. Palisaitis, N. Hellgren, F.F. Klimashin, N. Ghafoor, I. Zhirkov, C. Azina, J.-L. Battaglia, A. Kusiak, M.A. Sortica, J.E. Greene, L. Hultman, I. Petrov, P.O.Å. Persson, J. Rosen, Microstructure and materials properties of understoichiometric TiB_x thin films grown by HiPIMS, *Surf. Coat. Technol.* 404 (2020) 126537.
 - [10] T. Fiantok, N. Koutná, D.G. Sangiovanni, M. Mikula, Ceramic transition metal diboride superlattices with improved ductility and fracture toughness screened by ab initio calculations, *Sci. Rep.* 13 (1) (2023) 12835.
 - [11] R. Hahn, A.A. Tymoszyk, T. Wojcik, E. Ntemou, O. Hunold, P. Polcik, S. Kolozsvári, D. Primetzhof, P.H. Mayrhofer, H. Riedl, Unraveling the superlattice effect for hexagonal transition metal diboride coatings, *Scr. Mater.* 235 (2023) 115599.
 - [12] N. Hellgren, A. Sredenscheck, A. Petruinis, J. Palisaitis, F.F. Klimashin, M.A. Sortica, L. Hultman, P.O. Persson, J. Rosen, Synthesis and characterization of TiB_x ($1.2 \leq x \leq 2.8$) thin films grown by DC magnetron co-sputtering from TiB_2 and Ti targets, *Surf. Coat. Technol.* 433 (2022) 128110.
 - [13] C. Engström, T. Berlind, J. Birch, L. Hultman, I. Ivanov, S. Kirkpatrick, S. Rohde, Design, plasma studies, and ion assisted thin film growth in an unbalanced dual target magnetron sputtering system with a solenoid coil, *Vacuum* 56 (2) (2000) 107–113.
 - [14] J. Birch, M. Severin, U. Wahlström, Y. Yamamoto, G. Radnoczi, R. Riklund, J. E. Sundgren, L.R. Wallenberg, Structural characterization of precious-mean quasiperiodic Mo/V single-crystal superlattices grown by dual-target magnetron sputtering, *Phys. Rev. B* 41 (15) (1990) 10398–10407.
 - [15] B. Bakht, D. Primetzhof, E. Pitthan, M.A. Sortica, E. Ntemou, J. Rosen, L. Hultman, I. Petrov, G. Greczynski, Systematic compositional analysis of sputter-deposited boron-containing thin films, *J. Vac. Sci. Technol. A: Vacuum, Surfaces, and Films* 39 (6) (2021) 063408.
 - [16] J. Palisaitis, Use of cleaved wedge geometry for plan-view transmission electron microscopy sample preparation, *MRT.* 84 (12) (2021) 3182–3190.
 - [17] A. Devishvili, K. Zhernenkov, A.J. Dennison, B. Toperverg, M. Wolff, B. Hjörvarsson, H. Zabel, SuperADAM: Upgraded polarized neutron reflectometer at the Institut Laue-Langevin, *Rev. Sci. Instrum.* 84 (2) (2013).
 - [18] P. Mayrhofer, C. Mitterer, J.G. Wen, J.E. Greene, I. Petrov, Self-organized nanocolumnar structure in superhard TiB_2 thin films, *Appl. Phys. Lett.* 86 (2005) 131909.
 - [19] A. Mockutė, J. Palisaitis, B. Alling, P. Berastegui, E. Broitman, L.-Å. Näslund, N. Nedfors, J. Lu, J. Jensen, L. Hultman, J. Patscheider, U. Jansson, P.O.Å. Persson, J. Rosen, Age hardening in $(\text{Ti}_{1-x}\text{Al}_x)\text{B}_{2+\Delta}$ thin films, *Scr. Mater.* 127 (2017) 122–126.
 - [20] X. Li, B. Bakht, M.J. Jösaar, L. Hultman, I. Petrov, G. Greczynski, Toward energy-efficient physical vapor deposition: Routes for replacing substrate heating during magnetron sputter deposition by employing metal ion irradiation, *Surf. Coat. Technol.* 415 (2021) 127120.
 - [21] L. Tengdelius, G. Greczynski, M. Chubarov, J. Lu, U. Forsberg, L. Hultman, E. Janzén, H. Höglberg, Stoichiometric, epitaxial ZrB_2 thin films with low oxygen-content deposited by magnetron sputtering from a compound target: Effects of deposition temperature and sputtering power, *J. Cryst. Growth* 430 (2015) 55–62.
 - [22] A. Glavic, M. Björck, GenX 3: the latest generation of an established tool, *J. Appl. Crystallogr.* 55 (4) (2022) 1063–1071.
 - [23] J.A. Thornton, Influence of apparatus geometry and deposition conditions on the structure and topography of thick sputtered coatings, *J. Vac. Sci. Technol.* 11 (4) (1974) 666–670.
 - [24] A. Anders, A structure zone diagram including plasma-based deposition and ion etching, *Thin Solid Films* 518 (15) (2010) 4087–4090.